Available online at www.sciencedirect.com
ScienceDirect
International Journal of Thermal Sciences 48 (2009) 674–681
International Journal of Thermal Sciences
www.elsevier.com/locate/ijts

Meshless analysis of the substrate temperature in plasma spraying process

S.C. Wu [a,b,*], H.O. Zhang [a], Q. Tang [b,c], L. Chen [b], G.L. Wang [d]

[a] *State Key Laboratory of Digital Manufacturing and Equipment Technology, Huazhong University of Science and Technology, Wuhan, 430074 China*
[b] *Centre for Advanced Computations in Engineering Science (ACES), National University of Singapore, 9 Engineering Drive 1, 117576 Singapore*
[c] *State Key Laboratory of Advanced Design and Manufacturing for Vehicle Body, Hunan University, Changsha, 410082 China*
[d] *State Key Laboratory of Material Processing and Die & Mould Technology, Huazhong University of Science and Technology, Wuhan, 430074 China*

Received 22 October 2007; received in revised form 16 June 2008; accepted 16 June 2008

Available online 14 July 2008

Abstract

The substrate temperature plays a very important role in coating formation and its quality during the thermal spraying. Heating effect of the plasma and particle flux on the substrate is explored in detail in terms of different spraying distances using the meshless local Petrov–Galerkin method (MLPG). Based on this approach, a 3D transient heat transfer model is derived rigorously, in which the moving least-squares (MLS) method is introduced to construct the shape functions. A quartic spline function is selected as the weight function of the MLS scheme and also the test function for the discretized weak form, in which the penalty technique is used to treat the essential boundary conditions. For comparison, the finite element method (FEM) is also adopted to solve the same problem. It is found that the computed temperature is in very good agreement with the empirical data and better than that obtained using FEM, which validates the meshless formulation. Both numerical and experimental results indicate that the spraying distance has a crucial influence on heating effect of the plasma jet and particle flux onto the substrate.

Keywords: Meshless method; Plasma spraying; Spraying distance; Substrate temperature

1. Introduction

Plasma spraying process is basically the spraying of molten or heat softened powder on a substrate surface to be rapidly cooled for a coating [1]. It behaves a complex, dynamic and multi-parameters property, which complicates the temperature profile across the surface and through the substrate and coatings [2,3]. Heating effect on the substrate or coating is mainly attributed to the impinging plasma jet and the particle flux. In the impact on a substrate surface, the particles are generally deformed, rapidly cooled and solidified, and simultaneously transfer the heating energy into the substrate [4,5]. Hot molten or partially molten particles quench rapidly and flow and adhere better while impacting on a warm, dry surface with similar physical property than a reverse one. Therefore, the substrate temperature becomes a crucial factor especially when ceramics is deposited onto metals under the generation of residual stresses, which decisively influences the formation and quality of coatings [6]. This probably results in the degradation, oxidation, and shrinkage/expansion of the substrate, which inversely affects the properties of coatings [7,8]. In addition, due to complex combinations of operating parameters and transient high temperature gradient inside the particles and substrates, experimental and mathematical characterizations of temperature and resulted gradient (temperature gradient, thermal strain and stress) inter-relationships are actually of considerable difficulty [9]. Numerical methods can rapidly explore the physical behaviors at specific space and any time under arbitrary technological conditions.

As a well-developed numerical method, the finite element method (FEM) has been widely applied to obtain numerical solutions of various problems in engineering and science over the past decades. Unfortunately, FEM has some inherent shortcomings in relation with element distortion, meshing and remeshing, etc. mainly due to the strong reliance on element meshes. To avoid these drawbacks, meshless methods (also called meshfree methods) have been developed and remarkable progress has been made. Attracting increasing research attentions in both

* Corresponding author. Tel.: +65 65164797; fax: +65 65164795.
E-mail address: wushengchuan@gmail.com (S.C. Wu).

1290-0729/$ – see front matter
doi:10.1016/j.ijthermalsci.2008.06.011

Nomenclature

A	moment matrix defined in Eq. (5) weak form
B	matrix defined in Eq. (6)
C	capacitance matrix in Eq. (19)
c	specific heat coefficient ..... $\mathrm{J\,kg^{-1}\,^{\circ}C^{-1}}$
F	load vector defined in Eq. (19)
h	convection coefficient ..... $\mathrm{W\,m^{-2}\,^{\circ}C^{-1}}$
K	conduction matrix
k	thermal conductivity ..... $\mathrm{W\,m^{-1}\,^{\circ}C^{-1}}$
l	sequence number of test function
L_e	average nodal distance ..... m
m	node numbers for MLS approximation
N	total filed node of problem domain
p	basis function
Q	internal heat source intensity ..... $\mathrm{W\,m^{-3}}$
q_Γ	given heat flux on 2nd boundary ..... $\mathrm{W\,m^{-2}}$
R_0	radial characteristic coefficient boundary
r	radial distance ..... m
$\dot{\mathbf{q}}, \dot{T}$	temperature derivative with time ..... $^{\circ}\mathrm{C\,t^{-1}}$
T_a, T_0	ambient and initial temperature ..... °C
T_Γ	given temperature on 1st boundary ..... °C
t	time ..... s
v	test function in the weak form
w	MLS weight function
x	rectangular coordinate (x, y, z)

Greek symbols

Φ	shape function
Ω_s	local integration domain
ϕ	heat source distribution ..... $\mathrm{W\,m^{-2}}$
ϕ_0	axial value of heat flux ..... $\mathrm{MW\,m^{-2}}$
ρ	material density ..... $\mathrm{kg\,m^{-3}}$
α	penalty factor
Δt	stable time step ..... s
$\Gamma_1, \Gamma_2, \Gamma_3$	three types of global boundaries
$\Gamma_{s1}, \Gamma_{s2}, \Gamma_{s3}$	three types of sub-boundaries

Subscripts

I, J	nodal sequence number
n	unit outward normal to boundary
s	interpolation sub-domain
x, y, z	components in x, y, z directions

Superscripts

T	transpose operator
h	function approximation

academia and engineering in recent years, meshless methods have successfully attempted to solve various solid and fluid mechanics and heat transfer problems [10–12]. Among all these meshless methods, the element-free Galerkin method (EFG) [10] and the meshless local Petrov–Galerkin method (MLPG) [11] are considered to be promising.

As for the thermal process of the plasma spraying, there have been numerous publications concerning the numerical and experimental studies on the heating of plasma jet and the coatings/substrate, actually few papers published so far concentrate on the confirmation by comparisons between numerical and experimental measures of temperature and its gradient. The present work attempts to utilize the novel MLPG to investigate heating effect of the impinging plasma jet or particle flux onto the substrate under different spraying distances. Computational results are compared with experimental results and those obtained from FEM, which validate the meshless formulation. This can help the full understandings of the coating elaboration and the heat input prediction. The ultimate goal is to forecast the stress and/or strain field during/after the spraying process so that hot cracks can be alleviated to the most extent.

First, a meshless heat transfer model is established based on the MLPG procedure. In order to evaluate reliability and accuracy, the scaling parameter of local quadrature domain and the nodal distribution are studied in detail. In addition, experiments of the plasma spraying and finite element analysis are also conducted to confirm these results. Finally, temperature distribution and evolution of the substrate are solved to evaluate the heating effect of the plasma jet or particle flux under different spraying distances.

2. Meshless mathematical model

2.1. Shape function construction

The moving least-squares (MLS) approximation is generally considered to be one of the best schemes to interpolate data in the problem domain with a desired accuracy, and therefore is also adopted in the present procedure [13]. The unknown function $T(\mathbf{x})$ is approximated by $T^h(\mathbf{x})$ at interested point $\mathbf{x}$ as:

$$T^h(\mathbf{x}) = \sum_{j=1}^{m} p_j(\mathbf{x}) a_j(\mathbf{x}) = \mathbf{p}^{\mathrm{T}}(\mathbf{x})\mathbf{a}(\mathbf{x}) \tag{1}$$

where the superscript T is the matrix transpose operator, and

$$\mathbf{x}^{\mathrm{T}} = [\,x, \quad y, \quad z\,], \qquad \mathbf{p}^{\mathrm{T}} = [\,1, \quad x, \quad y, \quad z\,]$$
(for complete order of $m = 4$) (2)

Note that the coefficient vector $\mathbf{a}(\mathbf{x})$ in Eq. (1) are functions of space coordinates $\mathbf{x}$. The coefficient $a_j(\mathbf{x})$ can be obtained by minimizing the functional J:

$$J(\mathbf{x}) = \sum_{i=1}^{n} w(\mathbf{x} - \mathbf{x}_i)\left[\mathbf{p}^{\mathrm{T}}(\mathbf{x})\mathbf{a}(\mathbf{x}) - T_i\right]^2 \tag{3}$$

in which $w(\mathbf{x} - \mathbf{x}_i)$ is a nonzero weight function, T_i is the nodal temperature parameter, and n is the number of nodes in the local support domain of the interested point $\mathbf{x}$.

The stationary of functional J with respect to $\mathbf{a}(\mathbf{x})$ leads to:

$$\mathbf{a}(\mathbf{x}) = \mathbf{A}^{-1}(\mathbf{x})\mathbf{B}(\mathbf{x})\mathbf{T} \tag{4}$$

where $\mathbf{T}$ is the vector that collects the nodal parameters of temperature field in the support domain, and $\mathbf{A}(\mathbf{x})$ is the called the weighted *moment matrix* defined by:

$$\mathbf{A}(\mathbf{x})_{m\times m} = \sum_{i=1}^{n} w(\mathbf{x}-\mathbf{x}_i)\mathbf{p}(\mathbf{x}_i)\mathbf{p}^{\mathrm{T}}(\mathbf{x}_i), \tag{5}$$

$$\mathbf{B}(\mathbf{x})_{m\times n} = \big[w(\mathbf{x}-\mathbf{x}_1)\mathbf{p}(\mathbf{x}_1) \quad w(\mathbf{x}-\mathbf{x}_2)\mathbf{p}(\mathbf{x}_2) \quad \ldots \quad w(\mathbf{x}-\mathbf{x}_n)\mathbf{p}(\mathbf{x}_n)\big] \tag{6}$$

Substituting Eq. (4) back into Eq. (1), the MLS approximation is obtained as

$$T^h(\mathbf{x}) = \sum_{I=1}^{n} \Phi_I(\mathbf{x})T_I = \boldsymbol{\Phi}^{\mathrm{T}}(\mathbf{x})\mathbf{T} \tag{7}$$

where $\boldsymbol{\Phi}_I(\mathbf{x})$ is the MLS shape function, which is defined as:

$$\boldsymbol{\Phi}_I(\mathbf{x}) = \sum_{j=1}^{m} \mathbf{p}_j(\mathbf{x})\big[\mathbf{A}^{-1}(\mathbf{x})\mathbf{B}(\mathbf{x})\big]_{jI} = \mathbf{p}^{\mathrm{T}}\mathbf{A}^{-1}\mathbf{B}_I \tag{8}$$

and its first derivatives with respect space coordinates are

$$\boldsymbol{\Phi}_{I,\mathbf{x}}(\mathbf{x}) = \mathbf{p}^{\mathrm{T}}_{,\mathbf{x}}\cdot\mathbf{A}^{-1}\cdot\mathbf{B}_I + \mathbf{p}^{\mathrm{T}}\cdot(\mathbf{A}^{-1})_{,\mathbf{x}}\cdot\mathbf{B}_I + \mathbf{p}^{\mathrm{T}}\cdot\mathbf{A}^{-1}\cdot(\mathbf{B}_I)_{,\mathbf{x}} \tag{9}$$

It should be noted that the smoothness of the shape function is mainly determined by the weight function w. The selection of an appropriate weight function is crucial to the MLPG. It should be nonzero over the local support of node I and constructed so that a unique solution $\mathbf{a}(\mathbf{x})$ is guaranteed. More importantly, it should decrease with the increase of the distance from $\mathbf{x}$ to $\mathbf{x}_I$. In this paper, a quartic spline function [11] is adopted as the MLS weight function at the interested point $\mathbf{x}$:

$$w(\mathbf{x}-\mathbf{x}_I) \equiv w(r_x)w(r_y)w(r_z) = w_x w_y w_z \tag{10}$$

and its corresponding derivatives are expressed as:

$$w_{,x} = \frac{\mathrm{d}w_x}{\mathrm{d}x}w_y w_z, \qquad w_{,y} = \frac{\mathrm{d}w_y}{\mathrm{d}y}w_x w_z$$
$$w_{,z} = \frac{\mathrm{d}w_z}{\mathrm{d}z}w_x w_y \tag{11}$$

2.2. Local symmetric weak form (LSWF)

Consider a temperature field in homogeneous and isotropic solid Ω bounded by Γ as shown in Fig. 1. It is governed by the following partial differential equation and a set of boundary and initial conditions:

$$k\nabla^2 T(\mathbf{x}) + Q_v = \rho c\dot{T} \quad \Omega \tag{12}$$
$$T = T_\Gamma \quad \Gamma_1 \tag{13}$$
$$-kT_{,n} = q_\Gamma \quad \Gamma_2 \tag{14}$$
$$-kT_{,n} = h[T - T_a] \quad \Gamma_3 \tag{15}$$
$$T = T_0 \quad t = 0 \tag{16}$$

where k is the conductivity, $\dot{T}$ is the temperature derivative with respect to time, Q_v is internal heat source, c is the specific heat, ρ is the mass density, T_Γ and q_Γ are the given temperature and heat flux, h is the convection coefficient, T_a and T_0 are ambient and initial temperature, and n is components of unit outward normal to the boundary Γ.

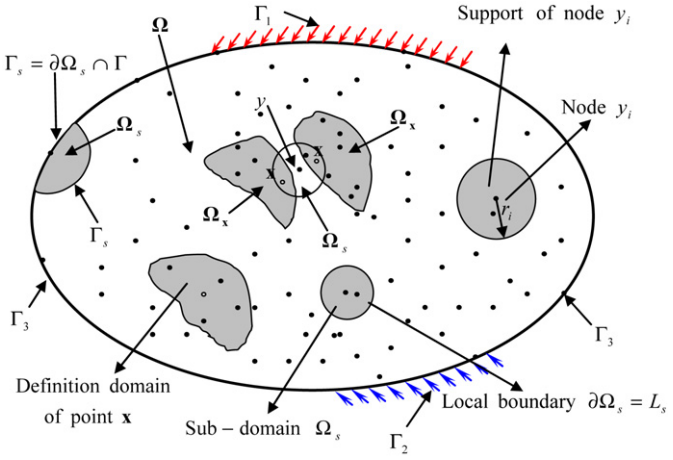

Fig. 1. A problem domain and boundaries for the MLPG. The definition domain $\Omega_{\mathbf{x}}$ covers all nodes whose weight functions are nonzero, the source point y is the union of all $\Omega_{\mathbf{x}}$, and the support of source point y_i is a sub-domain in which w_i is nonzero.

To enforce the essential boundary conditions an effective method of a penalty parameter α [12] is introduced into the discretized form.

Thus a local unsymmetrical form can be written as below:

$$\int_{\Omega_s}\big(k\nabla^2 T + Q_v - \rho c\dot{T}\big)v\,\mathrm{d}\Omega - \alpha\int_{\Gamma_{s1}}(T - T_\Gamma)v\,\mathrm{d}\Gamma = 0 \tag{17}$$

Unlike the conventional Galerkin method where the trial and test functions come from the same space, the MLPG introduces the trial and test functions from different function spaces. Also note that in the MLPG approach, the test function cannot vanish on the boundary where the EBCs are specified [11].

Using integration by parts and Green's theorem in Eq. (17) yield the local symmetric weak form (LSWF) in isotropic and homogenous solid and structures:

$$\begin{aligned}\int_{\Omega_s} kT_{,i}v_{l,i}\,\mathrm{d}\Omega + \alpha\int_{\Gamma_{s1}} Tv_l\,\mathrm{d}\Gamma - \int_{\Gamma_{s1}} kT_{,n}v_l\,\mathrm{d}\Gamma \\ + \int_{\Gamma_{s3}} hTv_l\,\mathrm{d}\Gamma + \int_{\Omega_s}\rho c\dot{T}v_l\,\mathrm{d}\Omega \\ = \int_{\Gamma_{s3}} hT_a v_l\,\mathrm{d}\Gamma - \int_{\Gamma_{s2}} q_\Gamma v_l\,\mathrm{d}\Gamma \\ + \alpha\int_{\Gamma_{s1}} T_\Gamma v_l\,\mathrm{d}\Gamma + \int_{\Omega_s} Q_v v_l\,\mathrm{d}\Omega\end{aligned} \tag{18}$$

where v_l denotes the test function in the lth set. The LSWF only requires that T and v are C^o continuous, which means mathematically that the approximation can produce a constant field function exactly. This requirements can significantly reduce the continuity of shape functions constructed using the MLS. To obtain the discrete forms, the MLS weight function w is referred to as the test function v_l in each local sub-domain, but

having the smaller sub-domain. Substituting Eq. (7) into the LSWF in Eq. (18) for N field nodes leads to the discretized system equations:

$$[\mathbf{K}]\{\mathbf{q}\} + [\mathbf{C}]\{\dot{\mathbf{q}}\} = \{\mathbf{F}\} \tag{19}$$

in which

$$K_{IJ} = \int_{\Omega_s} k\left(\frac{\partial \Phi_J(\mathbf{x})}{\partial x}\frac{\partial w(x,x_I)}{\partial x} + \frac{\partial \Phi_J(\mathbf{x})}{\partial y}\frac{\partial w(y,y_I)}{\partial y} + \frac{\partial \Phi_J(\mathbf{x})}{\partial z}\frac{\partial w(z,z_I)}{\partial z}\right)\mathrm{d}\Omega + \alpha\int_{\Gamma_{s1}} \Phi_J(\mathbf{x})w(\mathbf{x},\mathbf{x}_I)\,\mathrm{d}\Gamma - \int_{\Gamma_{s1}} k\frac{\partial \Phi_J(\mathbf{x})}{\partial n}w(\mathbf{x},\mathbf{x}_I)\,\mathrm{d}\Gamma + \int_{\Gamma_{s3}} h\Phi_J(\mathbf{x})w(\mathbf{x},\mathbf{x}_I)\,\mathrm{d}\Gamma$$

$$C_{IJ} = \int_{\Omega_s} \rho c \Phi_J(\mathbf{x})w(\mathbf{x},\mathbf{x}_I)\,\mathrm{d}\Omega$$

$$F_I = \int_{\Gamma_{s3}} hT_a w(\mathbf{x},\mathbf{x}_I)\,\mathrm{d}\Gamma - \int_{\Gamma_{s2}} q_\Gamma w(\mathbf{x},\mathbf{x}_I)\,\mathrm{d}\Gamma + \alpha\int_{\Gamma_{s1}} T_\Gamma w(\mathbf{x},\mathbf{x}_I)\,\mathrm{d}\Gamma + \int_{\Omega_s} Q_v w(\mathbf{x},\mathbf{x}_I)\,\mathrm{d}\Omega$$

and the vector of nodal temperature parameter is

$$\mathbf{q} = [q_1 \quad q_2 \quad \cdots \quad q_N]^{\mathrm{T}} \tag{20}$$

Using Crank–Nicolson difference technique for the time discreteness, Eq. (19) can be rewritten as below:

$$\left([\mathbf{K}] + \frac{2[\mathbf{C}]}{\Delta t}\right)\{\mathbf{T}\}_t = \left(\{\mathbf{F}\}_t + \{\mathbf{F}\}_{t-\Delta t}\right) - \left([\mathbf{K}] - \frac{2[\mathbf{C}]}{\Delta t}\right)\{\mathbf{T}\}_{t-\Delta t} \tag{21}$$

The stable time step Δt can be determined [14] by

$$\Delta t \leqslant L_e r_{\max} d_{\max}/2 \tag{22}$$

where $d_{\max}$ is the scaling parameter of local quadrature domain, $r_{\max}$ is the second-farthest distance for the local sub-domain and L_e is the averaged nodal distance.

2.3. Problem modeling

Steady and transient heat conductions of one column substrate with the radius 0.16 m and unit thickness are investigated in detail. Ambient temperature 25 °C is prescribed at the substrate edge. The specific heat and thermal conductivity of the material are 460 J/kg °C and 10 W/m °C respectively, and material density is 8200 kg/m^3. For simplicity, a distributed heat source is assumed to approximate the preheating effect of substrate using the micro-plasma arc with the spraying distance of 0.08 m as

$$\varphi(r) = 10800/\left[1 + (1000r/11)^2\right] \tag{23}$$

Here the radial expansion coefficient 11 and axial value of thermal flux 10800 W/m^2 are derived from the experimental evaluation.

Then the transient heat transfer analysis can be conducted after the steady-state simulation under the same material and initial-boundary conditions.

Previous works assumed that the thermal flux of the plasma jet was approximated by substandard Gauss profile. However, R. Bolot et al. [15] gave a general fitting of the thermal flux transferred with respect to the spraying distance

$$\varphi(r) = \frac{\varphi_0}{1 + (r/R_0)^2} \tag{24}$$

where ϕ_0 is the axial value of the thermal flux, r is the radial distance and R_0 is a coefficient that characterizes the radial expansion of plasma flux, which is related with the spraying distance d and can be approximated as [15]:

$$R_0 = 11(1000d/80)^{1.76} \tag{25}$$

The axis flux ϕ_0 can be evaluated through processing parameters

$$\varphi_0 = 0.228 + 5.57 \cdot 10^{-10} \cdot Fr^{0.052} \cdot Ar^{-1.64} \cdot d^{-2.55} \cdot p^{1.33} \cdot D^{-0.34} \tag{26}$$

in which Fr is the plasma gas flow rate, Ar is the argon volume fraction, d is the spraying distance, p is the electric power and D is the torch diameter.

The initial temperature can be obtained based on the flux distribution equation (23):

$$T(r,t)|_{t=0} = (25.0 + r), \quad r \in [0, 0.16] \tag{27}$$

3. Experimental conditions

The electric power is 30 kW and the plasma jet length is 195 mm and assumed to deliver an overall efficiency of 52%. For safety and cost, Ar and N_2 are selected as the working gas, and their flow rate are 20 and 10 slpm, respectively. The nozzle and injection diameters are 0.008 and 0.0018 m, respectively. The powder feeding rate is 0.076 g/s and the scanning speed is 0.1 m/s. Besides, the powder carrier gas rate is 200 slpm. The substrate is made of superalloy. The temperature detecting device used in this study is the IR-pyrometer typed Thermalert TX (Raytek Inc., USA) with a sampling rate 165 ms and a spot diameter size 10 mm. The device only provides local thermal information, and cannot cover the field of a large area without special scanning mechanism or increasing the number of IR-pyrometers. The numerical simulation can solve this situation efficiently and economically.

The GP-80 equipment is used in experiments and the pyrometer is fixed on the end arm of six-axis MOTOMAN-UP20 robot (RobotWorx, USA) and moves with the plasma torch. This permits the pyrometer to enlarge the detecting scope and its flexibility. During the detecting process, the pyrometer spot is aimed at one point of the substrate, pre-setting the distance 0.01 m away from the torch centerline. It should be specially

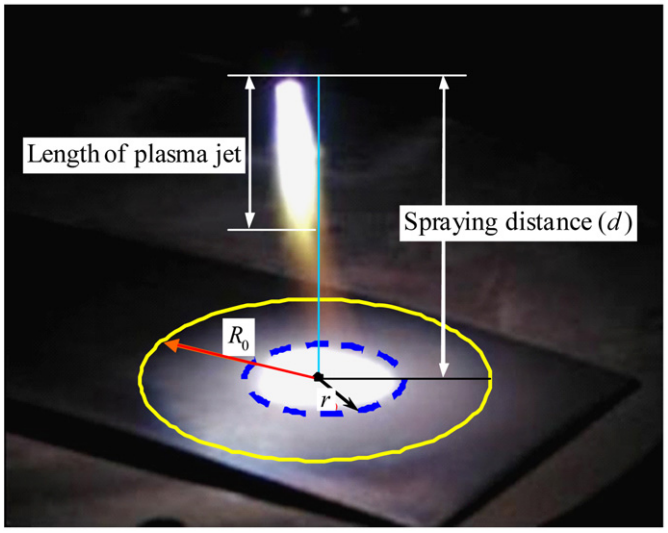

Fig. 2. Schematics of the plasma spraying with fixed point.

noted that the upper limit of the pyrometer is 300 °C . The measure detected is the temperature of substrate and that of the track in coatings which would be deposited in succession. According to our experiments, the spraying distance 100 mm is the best suitable for good deposition and coating elaboration.

Fig. 2 is the view of the plasma spraying process. Generally, the length of plasma jet is known as long as the experimental parameters and device are selected. The following study will focus on the variation of the spraying distance (d), which is used to present the heating effect of the thermal flux. Also note that the R_0 and r shown in Fig. 2 is only for simple schematics but not the accurate situation.

4. Numerical and experimental results

4.1. Steady state heat transfer

A robust in-house code based on FORTRAN is developed for the problem. For comparison, ABAQUS is also used to compute the temperature field of the substrate by a linear element with two nodes on its two ends. Figs. 3 and 4 give the temperature distribution along the radial direction from the present MLPG, FEM and the analytical ones with the spraying distances of 0.1 and 0.08 m, respectively. The average errors of MLPG and FEM to analytical solution are 0.241% and 4.99%, respectively, which shows that MLPG exhibits higher accuracy than FEM.

Table 1 shows the error and computational cost for different scaling parameters ($d_{\max}$) using four discretized models of 21, 41, 81 and 101 regularly distributed nodes.

Note that the parameters [12] (n_d for the number of the sub-partitions for numerical integration and α_i for ith nodal influence domain) are taken as: $n_d = 2$ and $\alpha_i = 2.5$.

It can be clearly seen that when 101 nodes are regularly distributed in the model, the relative errors are 0.28% and 2.61% for MLPG and FEM, and the computational time are 7.08 and 4.79 s, respectively. It can also be found that the scaling parameter varied from 2.00 to 2.75 can give acceptable results for

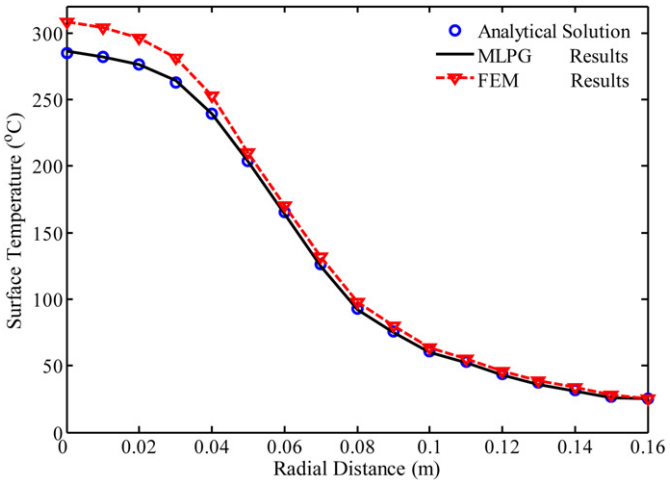

Fig. 3. Comparisons of computed temperature distribution along the radial direction for the MLPG, FEM and the analytical results with the spraying distance of $d = 0.1$ m.

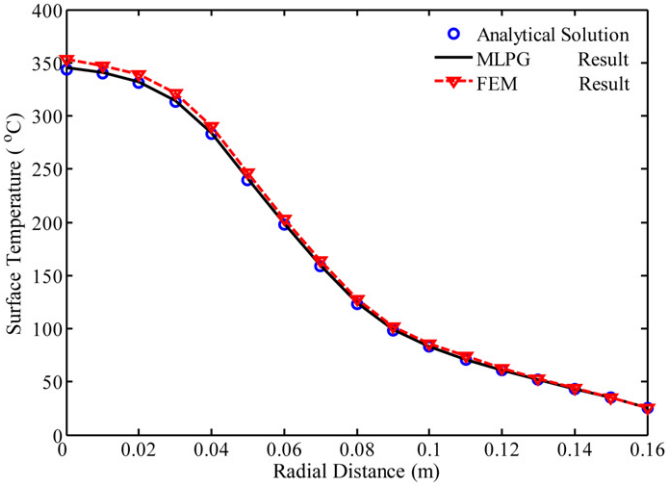

Fig. 4. Comparisons of computed temperature distribution along the radial direction for the MLPG, FEM and the analytical results with the spraying distance of $d = 0.08$ m.

quartic spline function. In addition, coupling computational accuracy and cost are optimized when $d_{\max}$ is set to be 2.75. The computational cost increases significantly with the increase of the scaling parameter and the number of nodes. Similar to the FEM, the ill nodal distribution in the MLPG may also cause bigger error and decrease the efficiency.

Comparisons from Figs. 3 and 4 and Table 1 show that the MLPG model for heat transfer is valid soundly. The convergence of the MLPG is also better than that of the FEM. This is because the MLS shape functions have higher order continuity. Also note that only the linear basis is used in the MLS approximation in the analysis.

4.2. Unsteady state heat transfer

Since the arrangement of 21 nodes and the numerical parameters of $d_{\max} = 2.75$, $n_d = 2$ and $\alpha_i = 2.5$ are effective enough to obtain very satisfactory results, the transient computation is

Table 1
Relative error and computational cost with different scaling parameters and nodal distributions

Scaling	21 nodes		41 nodes		81 nodes		101 nodes	
(d_{max})	Error (%)	Time (s)	Error (%)	Time (s)	Error (%)	Time (s)	Error (%)	Time (s)
2.00	17.98	0.99	6.87	1.74	0.73	4.67	0.25	6.89
2.25	1.61	0.91	0.93	1.66	0.75	4.62	0.31	6.69
2.50	1.55	0.92	0.91	1.67	0.48	4.56	0.29	6.84
2.75	1.49	0.92	0.89	1.71	0.24	4.52	0.28	7.08
3.00	1.43	0.94	0.85	1.76	0.21	4.83	0.21	7.46

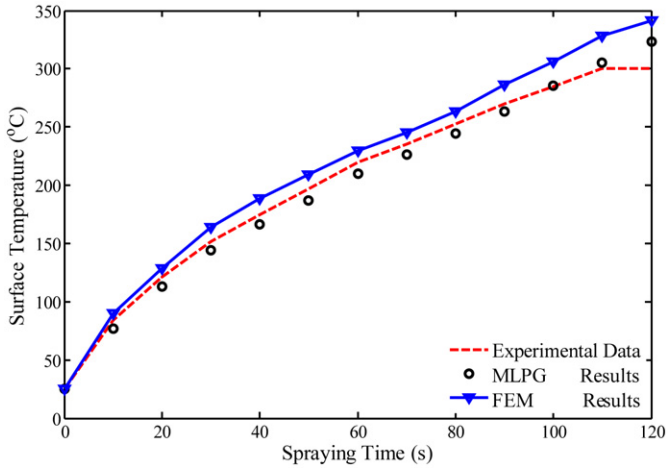

Fig. 5. Comparisons of computed temperature evolutions with the spraying distance of $d = 0.1$ m.

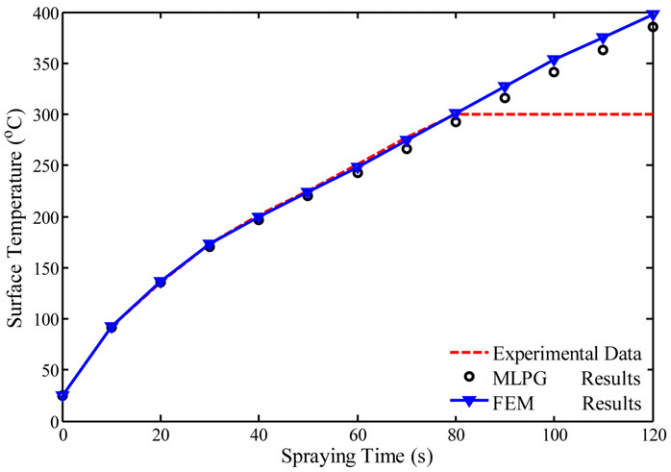

Fig. 6. Comparisons of computed temperature evolutions with the spraying distance of $d = 0.075$ m.

then carried out based on the steady-state analysis. The calculated temperature evolution of the interested point away from the central region 0.01 m, together with FEM and experimental results are plotted in Fig. 5.

According to Fig. 5, the temperature evolution of MLPG illustrates the same trend as that of FEM, and also coincides with experimental measures. The temperature value from the MLPG is less than that from the FEM, suggesting that the accuracy of the MLPG is bigger than that of the FEM in theory. Especially, the beeline section in Fig. 5 indicates that the temperature has exceeded the upper limit of the pyrometer. Thus, the numerical technique can forecast the information at any point and any time under arbitrary conditions in the absence of experimental measures. Finally, the whole field data is procurable only from the computation.

For more information, Fig. 6 further gives the computed temperature distributions of both the MLPG and the FEM with the shorter spraying distance of 0.075 m. Note also that the experimental data is not available due to exceeding the upper temperature limit of the pyrometer. It is found that decreasing the spraying distance leads to the rapid increase in temperature of substrate. Together with experiments, the impinging plasma jet actually gives the main contribution to heating the substrate.

These findings again validate the mathematical formulation of heat transfer derived from the MLPG procedure. Moreover, it can effectively analyze the transient heating effect in the substrate during the plasma spraying without the experimental results, thus providing more valuable information in the plasma spraying process.

4.3. Heating effect analysis

It is well known that the spraying distance is the most important factor for the final coating formation and quality in the spraying process. It determines the maximum flux basically including the plasma jet and the particle flux, and therefore has an unassailable influence on the temperature evolution of the substrate or coatings. Generally, the plasma jet provides more contribution to the temperature raise when the spraying distance is less than or equal to the length of plasma jet. When the spraying distance is bigger than the length of plasma jet, the particle flux is mostly responsible for heating the substrate. The contributions of the particle flux are presented in the following sections. Fig. 7 (a)–(c) gives the time history curves of the substrate temperature under different spraying distances of 0.15, 0.20 and 0.25 m, respectively.

It can be seen from Figs. 5–7 that the numerical results obtained from the MLPG are in good agreement with those from the experiments. Specially, the substrate temperature decreases significantly with the increasing of the spraying distance. This is mainly due to reducing the impinging plasma jet onto the substrate and the temperature will mainly depend on thermal impact of the particle flux. In detail, the temperature of substrate would reach the upper limit of the pyrometer only at the time of 116 s when the spraying distance is 0.1 m, as shown in Fig. 5. When the spraying distance is increased to be 0.15 m, the final temperature arrives at 264.5 °C in three minutes, as shown in Fig. 7(a). 207.6 °C can be obtained when $d = 0.2$ m in three minutes as shown in Fig. 7(b). Fig. 7(c) shows that the

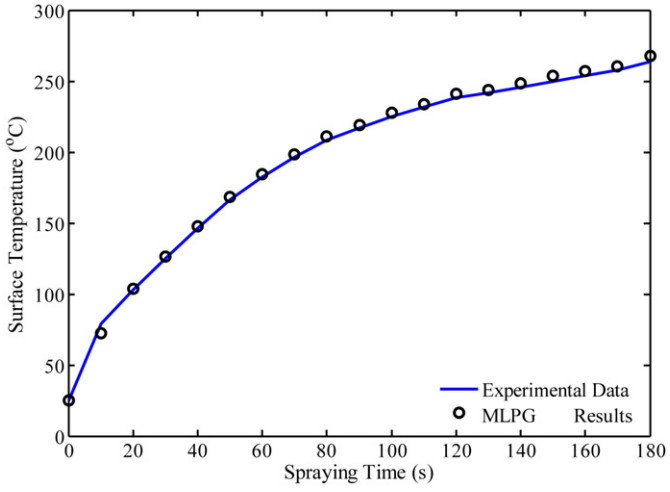

(a)

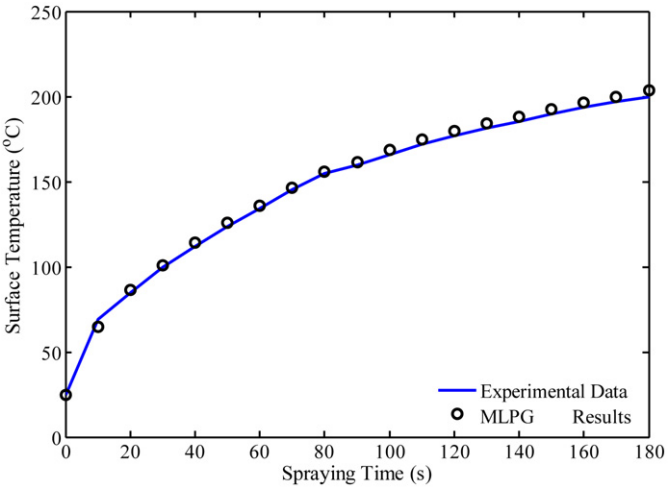

(b)

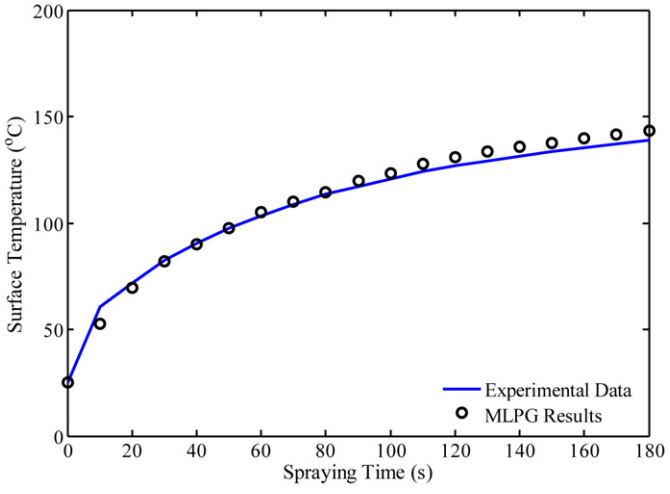

(c)

Fig. 7. (a) Heating effect of the impinging plasma jet with the spraying distance of $d = 0.15$ m. (b) Heating effect of the impinging plasma jet with the spraying distance of $d = 0.2$ m. (c) Heating effect of the impinging plasma jet with the spraying distance of $d = 0.25$ m.

substrate temperature is only 139.3 °C while the spraying distance is $d = 0.25$ m. Our experiments also show that the particle flux is mainly responsible for the temperature evolution when the plasma arc is gradually away from the substrate or coatings. Therefore, it is very important for engineers to pursue the optimal spraying distance for better heat transfer control.

In conclusion, both numerical and experimental results indicate that the spraying distance has a crucial influence on the heating effect of the impinging plasma jet or particle flux. The temperature variation and distribution of the substrate determine the final coatings shape and performance. This will help to select the suitable spraying distance to obtain the high quality coatings.

During the steady- and unsteady-state numerical implementation, less troublesome efforts have to be made for data preparation and additional post-processing, which certainly decreases the analysis cost of the MLPG.

5. Conclusions

A meshless formulation for heat transfer problems is derived using the MLPG approach. The MLS scheme is used to construct the shape functions. The penalty method is then introduced to enforce the essential boundary conditions due to the absence of delta function property of the MLS shape functions. The quartic spline function used in the MLS scheme is also chosen as the test function in obtaining the weak form. Numerical results show that MLPG can be applied to solve heat transfer of the substrate in the plasma spraying, and several remarks can be made as follows:

1. The optimal $d_{\max} = 2.75$ selected in this paper and the quartic spline weight function are valid to improve the accuracy, convergence and reliability.
2. Compared with FEM, the MLPG can achieve accuracy and less data preparation required, therefore reducing the analysis cost significantly.
3. The spraying distance has a strong influence on heating effect of the plasma jet or particle flux onto the substrate or coatings. Together with the length of plasma jet, it is very helpful and crucial to select the optimal spraying distance for better coating conformability and quality.

Acknowledgements

The support of the National Natural Science Foundation of China (Nos.: 50474053, 50475134 and 50675081) and 863 project (No.: 2007AA042142) is gratefully acknowledged. The authors also give sincerely thanks to Dr. W.S. Xia and the Centre for ACES, National University of Singapore, and the Singapore–MIT Alliance.

References

[1] L. Pawlowski, Temperature distribution in plasma sprayed coatings, Thin Solid Films 81 (1981) 79–88.

[2] Y. Bao, T. Zhang, D.T. Gawne, Non-steady State heating of substrate and coating during thermal-spray deposition, Surface and Coatings Technology 194 (2005) 82–94.
[3] G. Mariaux, A. Vardelle, 3D time-dependent modeling of the plasma spray process: Part 1: Flow modeling, International Journal of Thermal Sciences 44 (2005) 357–366.
[4] R. Bolot, J. Li, R. Bonnet, C. Mateus, C. Coddet, Modeling of the substrate temperature evolution during the APS thermal spray process, in: C. Moreau, B. Marple (Eds.), Thermal Spray 2003: Advancing the Science and Applying the Technology, ASM International, Materials Park, OH, USA, 2003, pp. 949–954.
[5] P. Fauchais, A. Vardelle, Heat mass and momentum transfer in coating formation by plasma spraying, International Journal of Thermal Sciences 39 (2000) 852–870.
[6] S. Sampath, X.Y. Jiang, J. Matejicek, A.C. Leger, A. Vardelle, Substrate temperature effects on splat formation, microstructure development and properties of plasma sprayed coatings. Part I, Materials Science and Engineering A 272 (1999) 181–188.
[7] C.J. Li, J.L. Li, W.B. Wang, The effect of substrate preheating and surface organic covering on splat formation, in: C. Coddet (Ed.), Thermal Spray 2001: Meeting the Challenges of the 21st Century, ASM International, Materials Park, OH, USA, 1998, pp. 437–480.
[8] J.R. Davis, Handbook of Thermal Spray Technology, ASM International, Materials Park, OH, 2004.
[9] L. Pawlowski, The Science and Engineering of Thermal Spray Coatings, John Wiley & Sons, 1995.
[10] T. Belytschko, Y.Y. Lu, L. Gu, Element-free Galerkin methods, International Journal for Numerical Method and Engineering 37 (1994) 229–256.
[11] S.N. Atluri, S.P. Shen, The Meshless Local Petrov–Galerkin (MLPG) Method, Tech Science Press, Los Angeles, 2002.
[12] G.R. Liu, Y.T. Gu, An Introduction to Meshless Methods and Their Programming, Springer Press, Dordrecht, Netherlands, 2005.
[13] P. Lancaster, K. Salkauskas, Surfaces generated by moving least squares methods, Mathematics of Computation 37 (1981) 141–158.
[14] P. Smolinski, T. Palmer, Procedures for multi-time step integration of element-free Galerkin methods for diffusion problems, Computers and Structures 77 (2000) 171–183.
[15] R. Bolot, M. Imbert, C. Coddet, Three dimensional transient modeling of the substrate temperature evaluation during the coating elaboration, in: Deutscher Verband Fur Schweiben (Eds.), Proc. ITSC2002, Thermal Spray Simulation, Essen 2002, pp. 979–984.